American Mineralogist, Volume 92, pages 468–480, 2007

Crystal chemistry of trioctahedral micas in alkaline and subalkaline volcanic rocks: A case study from Mt. Sassetto (Tolfa district, Latium, central Italy)

Angela Laurora,[1] Maria Franca Brigatti,[1,*] Annibale Mottana,[2] Daniele Malferrari,[1] and Enrico Caprilli[2]

[1]Dipartimento di Scienze della Terra, Università di Modena e Reggio Emilia, Modena, Italy
[2]Dipartimento di Scienze Geologiche, Università degli Studi Roma Tre, Roma, Italy

Abstract

This work provides a crystal-chemical description of trioctahedral micas from volcanic rocks (lavas, tuffs, ignimbrites, and xenoliths) outcropping at Mt. Sassetto (Tolfa district, Tuscan Province, central Italy). Mica crystals vary in composition from ferroan phlogopite to magnesian annite. Heterovalent octahedral substitutions are mainly related to Al^{3+}, Ti^{4+}, and, only in a few samples, to Fe^{3+}. The two main mechanisms regulating Ti inlet into the mica structure are the Ti-oxy [$^{VI}Ti^{4+VI}(Mg,Fe)^{2+}_{-1}(OH)^{-}_{-2}O^{2-}_{2}$] and Ti-vacancy [$^{VI}Ti^{4+VI}\square^{VI}(Mg,Fe)^{2+}_{-2}$] substitutions. In these micas, Ti content is the predominant crystal-chemical parameter and significantly affects octahedral and interlayer topology as well. Micas with the highest Ti contents deviate from the expected fractional crystallization trend in the Ti vs. Mg/(Mg + Fe_{tot}) diagram, possibly as a consequence of a variation in intensive parameters (T, P, f_{H_2}, f_{O_2}, f_{H_2O}) during crystallization in the magmatic chamber.

In micas with significant Fe^{3+} contents, the layer charge balance is accomplished by the following mechanisms: $^{VI}Fe^{2+VI}_{-3}Fe^{3+VI}_{2}\square$, $^{VI}Fe^{2+VI}_{-1}Fe^{3+}(OH)^{-}_{-1}O^{2-}$, and $^{VI}Fe^{2+VI}_{-1}Fe^{3+IV}Si^{4+IV}_{-1}Al^{3+}$. These micas show mean electron counts greater for the octahedral M2 site than for M1, and unit-cell parameters significantly smaller than usual for other micas. Atmospheric weathering is unlikely to produce the observed Fe oxidation. The Fe^{3+}-vacancy and Fe-oxy substitutions could represent secondary, re-equilibration effects related to post-eruptive water-rock hydrothermal processes (acid-sulfate alteration).

Keywords: Volcanic micas, central Italy, mica oxidation, hydrothermalism, crystal chemistry, Ti-substitutions, hydrothermalism

Introduction

The crystal chemistry of trioctahedral micas is deeply related to petrogenetic processes active during crystallization, as demonstrated by several studies pertaining to igneous and metamorphic environments (e.g., Brigatti and Guggenheim 2002; Guidotti and Sassi 2002; Cesare et al. 2003; Brigatti et al. 2005).

Some authors suggest that trioctahedral micas from volcanic environments change in composition as a function of the chemical system, temperature, and pressure. Moreover, according to some of them (Shane et al. 2003; Harangi et al. 2005), major elements such as Ti, Mg, and Fe support the reconstruction of the stratigraphic sequence in pyroclastic deposits. Only minimal attention has been devoted so far to the crystal-chemical parameters in micas from volcanic rocks that may be possible indicators of other petrogenetic processes. Only a few, very recent works (Brigatti et al. 2005; Mesto et al. 2006) have tried to relate the variation of certain crystal-chemical parameters in micas (e.g., the tetrahedral rotation angle, the distortion of tetrahedra and of octahedra, the sheet thickness) to regular changes in the chemical composition of the host rocks across a volcanic sequence, both effusive and pyroclastic.

As extensively demonstrated in the literature (Guidotti 1984; Redhammer et al. 1995, 2000, 2005), trioctahedral micas in the phlogopite–annite join are affected by different substitution processes, such as Tschermak substitutions (e.g., $^{VI}Mg^{2+}_{-1}{}^{VI}Al^{3+IV}Si^{4+IV}_{-1}Al^{3+}$; $^{VI}Mg^{2+VI}_{-1}Fe^{3+IV}Si^{4+IV}_{-1}Al^{3+}$; $^{VI}Fe^{2+VI}_{-1}Fe^{3+IV}Si^{4+IV}_{-1}Al^{3+}$; $^{VI}Mg^{2+VI}_{-1}Ti^{4+IV}Si^{4+IV}_{-2}Al^{3+}_{2}$), octahedral vacancies substitutions (e.g., $^{VI}Mg^{2+VI}_{-3}Al^{3+VI}_{2}\square$; $^{VI}Mg^{2+VI}_{-3}Fe^{3+VI}_{2}\square$; $^{VI}Fe^{2+VI}_{-3}Fe^{3+VI}_{2}\square$; $^{VI}Mg^{2+VI}_{-2}Ti^{4+VI}\square$) and oxy-substitutions (e.g., $^{VI}Mg^{2+VI}_{-1}Al^{3+}(OH)^{-}_{-1}O^{2-}$; $^{VI}Mg^{2+}_{-1}{}^{VI}Fe^{3+}(OH)^{-}_{-1}O^{2-}$; $^{VI}Fe^{2+VI}_{-1}Fe^{3+}(OH)^{-}_{-1}O^{2-}$; $^{VI}Mg^{2+VI}_{-1}Ti^{4+}(OH)^{-}_{-2}O^{2-}_{2}$). These substitutions affect different structural sites, since charge balance can be achieved either inside one site only or by involvement of several sites. Thus, the geometric variation of the mica layer as a result of a given chemical substitution is not always linear, and can be extremely complex. When addressing volcanic rocks subjected to secondary alteration processes (i.e., of hydrothermal or meteoric origin), different substitution mechanisms may mark a discrimination between an initial signature, dating back to processes occurred during the igneous phase of mica crystallization, and a subsequent signature, acquired during later alteration events, and thus associated with (re-)equilibration of the mica in its depositional environment. As a result, a complex crystal-chemical behavior could conveniently describe a complex genetic history.

This work will focus on the crystal-chemical features of micas in alkaline and subalkaline volcanic rocks from Mt. Sassetto (Tolfa district, Italy). These volcanic rocks are characterized by a complex petrologic and genetic history, and they are included in

* E-mail: brigatti@unimore.it

a well-studied, easy-to-map volcanic sequence, thus opening interesting opportunities for the assessment of the interrelationships between mica crystal chemistry and its genetic environment.

Material and methods

Samples

All the samples under study are from Mt. Sassetto, a hill in the northwestern corner of the Tolfa district (Fig. 1a). Volcanic rocks from the Tolfa district are very hard to characterize from a chemical and petrographic point of view because they bear a strong imprint of late hydrothermal acid-sulfate alteration. According to a wide range of studies from Negretti et al. (1966) to Jolivet et al. (1998), this hydrothermal effect, commonly observed to various extents over the entire district, is less enhanced in the Mt. Sassetto area.

At Monte Sassetto, the volcanic rocks are emplaced over a sedimentary substrate (Figs. 1a and 1b) and consist of ignimbrites and "chaotic tuffs" (Negretti et al. 1966), i.e., poorly consolidated benches holding agglomerates with heterogeneous blocks (from a few centimeters to a meter in size, either rounded or angular) in a poor "cineritic matrix" (i.e., volcanic ash). Acidic lava domes cut through the ignimbrite plateau that, based on field observations, was placed stratigraphically above the "chaotic tuffs." Tuffs, ignimbrites, and lavas contain two types of magmatic xenoliths. Type I xenoliths show a clear effusive origin and, from a structural and paragenetic point of view, are very similar to other Tolfa lavas. Type II xenoliths are latitic magma products resembling those of the Roman Perpotassic Province (Pinarelli 1991; Bertagnini et al. 1995).

In the Mt. Sassetto hill, "cineritic matrix" of "chaotic tuffs", ignimbrites, lavas, Type I and Type II xenoliths were sampled (Fig. 1b). Table 1 reports the complete list of the samples studied and some additional information on location and petrographic features.

X-ray fluorescence analysis

Very little information has been published about the size or bulk-rock chemical composition of the studied samples (see Table 2[1]). All samples, with the exception of MS9, MS10, and MS15, were analyzed following the methods by Franzini et al. (1975) and Leoni and Saitta (1976), using a Philips PW1480 X-ray fluorescence spectrometer, thus determining the concentrations of the major elements and of trace elements Ni, Co, Cr, V, Ce, Nd, Ba, La, Nb, Zr, Y, Sr, Rb, Pb, As, Zn, Cu, and S. Final accuracies are within 2–5% for major elements and within 10% for trace elements. Total Fe is reported as Fe_2O_3. Bulk-rock H_2O contents were obtained via thermal analysis (Seiko SSC 5200) in He gas flow.

[1] Deposit item AM-07-015, Tables 2, 3, 8, and 9 (much detail of the sample studies). Deposit items are available two ways: For a paper copy contact the Business Office of the Mineralogical Society of America (see inside front cover of recent issue) for price information. For an electronic copy visit the MSA web site at http://www.minsocam.org, go to the American Mineralogist Contents, find the table of contents for the specific volume/issue wanted, and then click on the deposit link there.

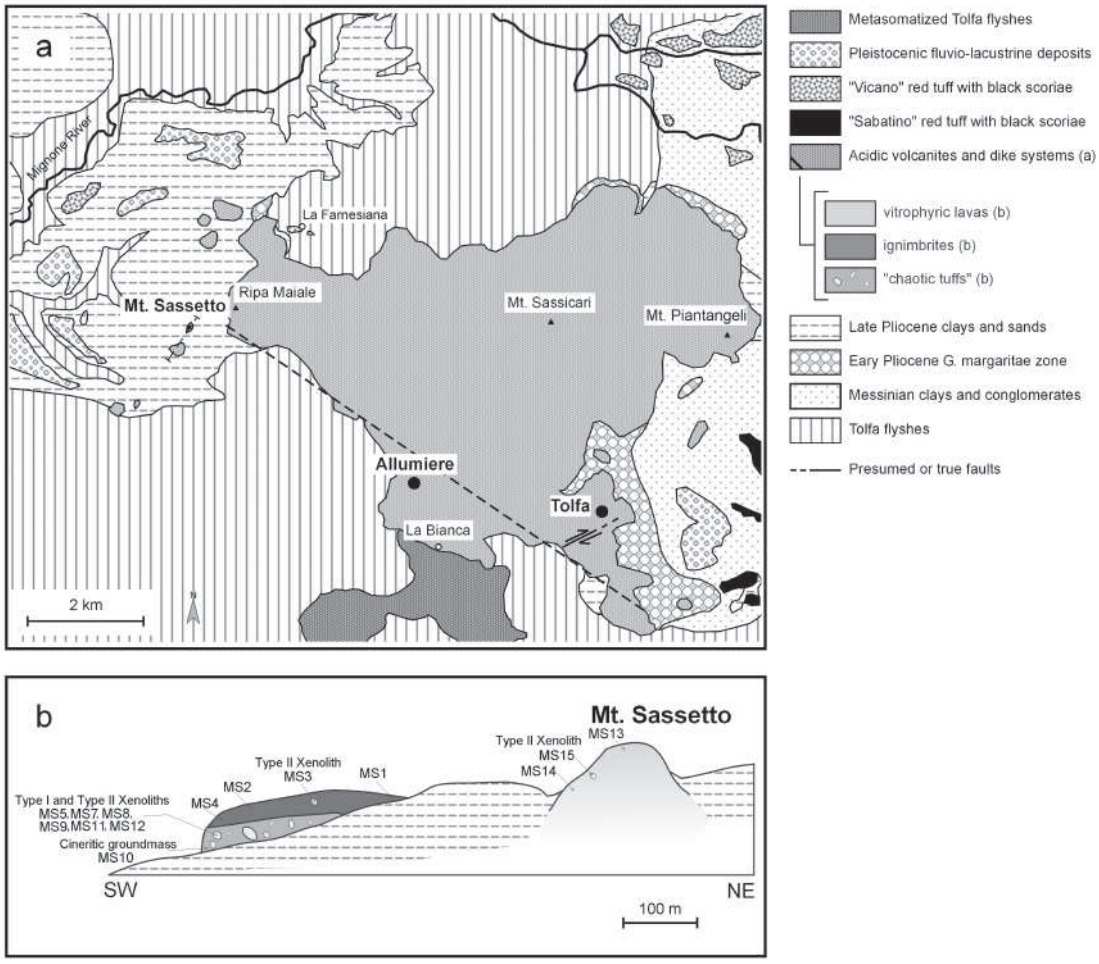

Figure 1. (**a**) Geologic map of the Tolfa area (modified after De Rita et al. 1997); (**b**) geologic section of the Mt. Sassetto sector (modified after Negretti et al. 1966).

TABLE 1. Petrographic features, minerals, rock type and location of Mt. Sassetto samples

Sample	Structure	Minerals	Rock type
MS1	Vitrophyric pseudofluidal with perlitic devitrified groundmass	Phenocrysts: sanidine, plagioclase, ortho- and clinopyroxene, mica Accessory phases: apatite, ilmenite Secondary phases: smectite, iron hydroxides	Ignimbrite—porous facies TOP
MS2	Vitrophyric pseudofluidal with perlitic devitrified groundmass	Phenocrysts: sanidine, plagioclase, ortho- and clinopyroxene, mica, ilmenite Accessory phases: apatite, titanomagnetite, quartz Secondary phases: smectite, iron hydroxides	Ignimbrite—porous facies MIDDLE
MS3	Doleritic	Sanidine, plagioclase, ortho- and clinopyroxene, mica, apatite (accessory), ilmenite (accessory) Secondary phases: smectite, iron hydroxides	Type II xenolith in Ignimbrite—porous facies
MS4	Vitrophyric with perlitic devitrified groundmass	Phenocrysts: sanidine, plagioclase, ortho- and clinopyroxene, mica, spinel Accessory phases: titanomagnetite, ilmenite Secondary phases: smectite, iron hydroxides	Ignimbrite—porous facies BASE
MS5	Doleritic	Plagioclase, sanidine, mica, clino- and orthopyroxene, apatite (accessory), ilmenite (accessory) Secondary phases: smectite, iron hydroxides	Type II xenolith in "chaotic tuffs"
MS7	Doleritic	Plagioclase, sanidine, mica, clinopyroxene, apatite (accessory) ilmenite (accessory), titanomagnetite (accessory) Secondary phases: smectite, iron hydroxides	Type II xenolith in "chaotic tuffs"
MS8	Doleritic	Plagioclase, sanidine, mica, clinopyroxene, apatite (accessory) ilmenite (accessory), titanomagnetite (accessory) Secondary phases: smectite, iron hydroxides	Type II xenolith in "chaotic tuffs"
MS9	Vitrophyric pseudofluidal with devitrified groundmass	Phenocrysts: sanidine, plagioclase, ortho- and clinopyroxene, mica Accessory phases: apatite, ilmenite Secondary phases: smectite, iron hydroxides	Hypocrystalline xenolith in "chaotic tuffs"
MS10	Vitrophyric with perlitic devitrified groundmass	Phenocrysts: sanidine, plagioclase, orthopyroxene, mica Accessory phases: ilmenite Secondary phases: smectite, iron hydroxides	"chaotic tuffs" - sample of the "cineritic matrix"
MS11	Doleritic	Plagioclase, mica, ortho- and clinopyroxene, apatite (accessory), ilmenite (accessory) Secondary phases: smectite, iron hydroxides	Type II xenolith in "chaotic tuffs"
MS12	Vitrophyric with perlitic devitrified groundmass	Phenocrysts: sanidine, plagioclase, ortho- and clinopyroxene, mica, quartz Accessory phases: ilmenite, titanomagnetite Secondary phases: smectite, iron hydroxides	Type I xenolith in "chaotic tuffs"
MS13	Vitrophyric with devitrified groundmass	Phenocrysts: sanidine, plagioclase, ortho- and clinopyroxene, mica Accessory phases: ilmenite Secondary phases: smectite, iron hydroxides	Lava dome
INNER PART MS14	Vitrophyric with devitrified groundmass	Phenocrysts: sanidine, plagioclase, ortho- and clinopyroxene, mica Accessory phases: ilmenite Secondary phases: smectite, iron hydroxides	Lava dome OUTER PART
MS15	Doleritic	Plagioclase, mica, orthopyroxene, quartz, ilmenite (accessory) Secondary phases: smectite, iron hydroxides	Type II xenolith in lava dome

Electron-microprobe analysis (EMPA)

The chemical composition of mica crystals was determined by wavelength-dispersive EMPA using an ARL-SEMQ microprobe at Modena and Reggio Emilia University. The chemical composition was obtained both on mica crystals in thin section (Table 3[1]) and on the same crystal selected for structure refinement (Table 4). For each crystal, several points were analyzed to check for sample homogeneity. Operating conditions were 15 kV accelerating voltage, 15 nA sample current, and 15 µm beam diameter. Analyses and data reduction were performed using the probe software package of Donovan (1995). The following standards were used: fluorite (F), sodalite (Cl), microcline (K), albite (Na), spessartine (Al, Mn), ilmenite (Fe, Ti), clinopyroxene (Si, Ca), olivine (Mg), paracelsian (Ba), and chromite (Cr). The F content was determined following the method reported by Foley (1989). No evidence of F volatilization was observed. Table 3[1] reports averaged analyses of different crystals from the same thin section and their relative standard deviations. Analyses of crystals coming from the same sample, but showing remarkable differences in their compositions (i.e., MS9 and MS12) were not averaged or averaged on different subgroups. Chemical formulae were determined following two different methods as reported in Brigatti et al. (2005). The first normalization procedure was

TABLE 4. Major element analyses (oxide wt%) and chemical formulae (apfu) of Mt. Sassetto mica crystals used in single-crystal X-ray diffraction study

Rock type	Ignimbrite			Type I xenoliths		Type II xenoliths							Tuffs	Lavas		
Sample	MS1	MS2	MS4	MS9	MS12	MS3(1)	MS3(2)	MS5	MS7	MS8(1)	MS8(2)	MS11	MS10	MS13	MS14(1)	MS14(2)
Chemical composition (oxide wt%)																
SiO_2	36.04	36.65	36.69	35.94	36.97	35.75	36.04	34.41	34.46	34.63	34.93	36.94	36.61	36.41	36.38	37.43
TiO_2	5.24	4.87	5.29	3.01	5.22	4.68	4.49	3.50	3.98	2.91	2.99	5.46	5.21	5.38	5.60	5.53
Al_2O_3	13.53	12.88	12.81	15.22	12.70	14.10	14.22	15.52	14.52	14.92	14.69	12.60	12.83	12.97	13.12	12.94
Fe_2O_3	0.00	0.00	0.00	0.00	0.00	0.00	0.00	0.00	12.47	11.77	11.97	0.00	0.00	0.00	0.00	0.00
Cr_2O_3	0.08	0.07	0.10	0.01	0.05	0.00	0.00	0.01	0.02	0.01	0.01	0.08	0.07	0.06	0.03	0.06
FeO	16.55	17.31	16.85	18.12	16.56	17.32	16.95	17.26	10.00	10.13	10.11	16.76	17.43	16.56	16.73	16.51
MnO	0.08	0.11	0.02	0.17	0.09	0.17	0.20	0.14	0.29	0.16	0.25	0.08	0.08	0.05	0.02	0.04
MgO	12.73	12.61	12.70	11.52	12.87	12.35	12.45	12.51	8.76	9.50	9.45	13.08	12.64	12.95	12.62	12.34
CaO	0.08	0.05	0.09	0.05	0.04	0.05	0.01	0.07	0.14	0.07	0.15	0.09	0.01	0.02	0.09	0.11
BaO	0.00	0.00	0.00	0.21	0.07	0.00	0.00	0.36	0.40	0.28	0.32	0.00	0.00	0.00	0.00	0.01
Na_2O	0.41	0.41	0.48	0.36	0.44	0.44	0.40	0.43	0.45	0.47	0.47	0.42	0.38	0.46	0.42	0.39
K_2O	9.28	8.73	8.93	9.00	9.32	9.44	9.30	9.17	8.76	9.10	9.03	9.22	9.40	9.27	9.33	9.26
F	1.63	1.97	1.85	1.82	1.48	1.20	1.33	1.18	1.83	1.45	1.03	1.21	0.94	1.87	1.50	1.45
Cl	0.01	0.00	0.02	0.05	0.02	0.02	0.02	0.02	0.00	0.00	0.00	0.00	0.00	0.01	0.01	0.01
H_2O	4.34	4.35	4.15	4.45	4.20	4.50	4.50	5.40	3.90	4.60	4.60	4.05	4.40	4.00	4.20	3.95
Sum	99.99	100.01	99.98	99.93	100.03	100.02	99.91	99.97	99.97	100.00	100.00	99.99	100.01	100.01	100.05	100.03
Unit-cell content recalculated on the basis of $O_{12-(x+y+z)}(OH)_xF_yCl_z$																
^{iv}Si	2.825	2.870	2.873	2.831	2.896	2.815	2.830	2.715	2.719	2.725	2.750	2.895	2.881	2.853	2.852	2.923
^{iv}Al	1.175	1.130	1.127	1.169	1.104	1.185	1.170	1.285	1.281	1.275	1.250	1.105	1.119	1.147	1.148	1.077
Sum	4.000	4.000	4.000	4.000	4.000	4.000	4.000	4.000	4.000	4.000	4.000	4.000	4.000	4.000	4.000	4.000
^{vi}Al	0.075	0.059	0.055	0.243	0.068	0.123	0.146	0.158	0.070	0.109	0.114	0.059	0.070	0.051	0.064	0.114
^{vi}Mg	1.487	1.472	1.482	1.352	1.502	1.449	1.457	1.471	1.030	1.114	1.109	1.528	1.482	1.513	1.475	1.436
$^{vi}Fe^{3+}$	0.000	0.000	0.000	0.000	0.000	0.000	0.000	0.000	0.740	0.697	0.709	0.000	0.000	0.000	0.000	0.000
$^{vi}Fe^{2+}$	1.085	1.134	1.103	1.194	1.085	1.140	1.113	1.139	0.660	0.667	0.666	1.098	1.147	1.085	1.097	1.078
$^{vi}Cr^{3+}$	0.005	0.005	0.006	0.001	0.003	0.000	0.000	0.001	0.001	0.000	0.001	0.005	0.005	0.004	0.002	0.004
$^{vi}Mn^{2+}$	0.005	0.007	0.001	0.011	0.006	0.011	0.013	0.009	0.019	0.011	0.017	0.005	0.005	0.003	0.001	0.003
$^{vi}Ti^{4+}$	0.309	0.287	0.311	0.178	0.307	0.277	0.265	0.208	0.236	0.172	0.177	0.322	0.308	0.317	0.330	0.325
Sum	2.966	2.963	2.959	2.980	2.972	3.001	2.994	2.985	2.757	2.770	2.792	3.018	3.018	2.973	2.969	2.960
^{xii}Ca	0.007	0.004	0.008	0.004	0.003	0.004	0.001	0.006	0.012	0.006	0.012	0.008	0.001	0.002	0.008	0.009
^{xii}Na	0.063	0.062	0.073	0.055	0.067	0.067	0.061	0.066	0.069	0.072	0.072	0.064	0.058	0.070	0.064	0.059
^{xii}K	0.928	0.872	0.892	0.904	0.931	0.948	0.932	0.923	0.882	0.914	0.907	0.922	0.943	0.927	0.933	0.923
^{xii}Ba	0.000	0.000	0.000	0.006	0.002	0.000	0.000	0.011	0.012	0.009	0.010	0.000	0.000	0.000	0.000	0.000
Sum	0.998	0.939	0.972	0.970	1.003	1.019	0.993	1.006	0.975	1.000	1.001	0.993	1.003	0.998	1.004	0.991
F	0.405	0.488	0.458	0.453	0.367	0.299	0.330	0.294	0.457	0.361	0.256	0.300	0.234	0.463	0.372	0.358
Cl	0.001	0.000	0.003	0.007	0.003	0.003	0.003	0.003	0.000	0.000	0.000	0.000	0.000	0.001	0.001	0.001
OH	1.135	1.136	1.084	1.169	1.097	1.182	1.178	1.421	1.026	1.208	1.208	1.059	1.155	1.045	1.098	1.029
O	10.459	10.376	10.456	10.371	10.534	10.517	10.489	10.282	10.517	10.432	10.535	10.641	10.612	10.490	10.529	10.612
Sum	12.000	12.000	12.000	12.000	12.000	12.000	12.000	12.000	12.000	12.000	12.000	12.000	12.000	12.000	12.000	12.000
Mean electron count																
M1 (Xref)	18.2(1)	18.65(2)	18.47(8)	18.32(9)	17.9(1)	18.78(8)	18.54(7)	17.8(1)	18.05(9)	16.65(9)	16.62(9)	18.7(1)	18.43(2)	18.7(1)	18.36(7)	18.47(5)
M2 (Xref)	18.1(1)	17.85(3)	18.05(8)	18.36(7)	17.9(1)	18.26(9)	17.98(7)	18.0(1)	18.95(7)	18.82(7)	19.09(9)	18.1(1)	18.20(4)	18.0(1)	17.95(6)	17.98(4)
M1+2M2 (Xref)	54.4	54.35	54.57	55.04	53.7	55.30	54.50	53.8	55.95	54.29	54.80	54.90	54.83	54.7	54.26	54.43
M1+2M2 (EMPA)	54.1	54.50	54.22	54.65	54.1	55.02	54.48	54.1	55.4	54.3	54.9	55.0	55.5	54.2	54.4	54.1
A(Xref)	18.29(9)	17.53(2)	18.18(8)	18.49(9)	18.6(1)	18.70(9)	18.48(7)	19.0(1)	18.69(9)	18.62(9)	18.7(1)	18.2(1)	18.56(4)	18.4(1)	18.1(1)	18.13(6)
A(EMPA)	18.46	17.34	17.90	18.23	18.61	18.84	18.39	19.00	18.44	18.75	18.82	18.37	18.59	18.41	18.58	18.38

Notes: Xref = single-crystal X-ray refinement; EMPA = electron microprobe analysis.

applied to crystals on thin sections (Table 3[1]), the second one was applied to crystals selected for single-crystal X-ray diffraction (XRD) study (Table 4).

X-ray-diffraction data

Mica crystals selected for structural investigation, were mounted on a Bruker X8-Apex fully automated four-circle diffractometer with Kappa geometry, ceramic X-ray tube KFF-Mo-2k-90 Fine Focus, and APEX 4K CCD area detector. An automatic data collection strategy was defined using the APEX2 software. The SMART package was used for unit-cell determination and for X-ray data collection. Redundant data were collected for an approximate sphere of reciprocal space and were integrated and corrected for background and Lorentz-polarization factors using the Bruker program SAINT+ (Bruker 1999a). The Bruker SADABS (Bruker 1999b) package was used to make the semi-empirical absorption correction. The crystal structure was refined using the SHELX-97 package of programs (Sheldrick 1997).

The unit-cell parameters of the measured micas and information related to X-ray data collection are reported in Table 5. Structure refinements were performed following the assumptions previously adopted by Brigatti et al. (2005) for ferroan phlogopite. Atomic-position parameters from Brigatti et al. (2005) were assumed as initial values to refine the 1*M* and $2M_1$ polytypes. Appropriate neutral scattering factors were used for both cationic and anionic positions. In the final cycles, anisotropic displacement parameters were refined for all atoms. Table 4 reports octahedral and interlayer mean electron counts (m.e.c.) from crystal-structure refinements and, for comparison, from electron microprobe measurements. Final refinements yielded the *R*(F) values reported in Table 5. The final calculated difference electron density maps did not reveal significant excesses in electron density above background. Tables 6a and 6b list relevant cation-anion bond lengths for 1*M* and $2M_1$ polytypes, respectively, and Table 7 presents selected geometrical parameters obtained from structure refinements. Atom coordinates and equivalent isotropic and anisotropic displacement factors are reported in Table 8[1]. Site occupancies derived by combining data from chemical analysis and from crystal-structure refinement are reported in Table 9[1].

RESULTS AND DISCUSSION

Petrographic features

Tuffs ("cineritic matrix"), Type I xenoliths, and ignimbrites from Mt. Sassetto vary in texture from porphyritic to vitrophyric pseudo-fluidal (Fig. 2a). A typical assemblage is constituted

TABLE 5. Unit-cell parameters and information related to X-ray data collection of Mt. Sassetto micas

Sample	Polytype	Space group	N_{unique}	R_{int} (%)	R_F (%)	Goodness of fit	θ_{min} (°)	θ_{max} (°)	*a* (Å)	*b* (Å)	*c* (Å)	β (°)	*V* (Å$_3$)
Ignimbrite													
MS1	$2M_1$	*C*2/*c*	997	2.73	2.64	0.970	4.41	26.27	5.3332(3)	9.2376(5)	20.069(1)	95.125(2)	984.78(9)
MS2	1*M*	*C*2/*m*	1112	2.97	2.84	0.983	4.08	34.54	5.3369(4)	9.2423(6)	10.1618(7)	100.222(2)	493.28(6)
MS4	$2M_1$	*C*2/*c*	1471	2.72	3.212	0.891	4.07	30.98	5.3368(3)	9.2377(6)	20.086(1)	95.128(4)	986.3(1)
Type I xenoliths													
MS9	1*M*	*C*2/*m*	1103	3.80	3.42	0.998	4.06	34.67	5.3304(2)	9.2277(4)	10.1918(4)	100.051(2)	493.61(3)
MS12	1M	*C*2/*m*	660	2.78	2.63	0.888	4.08	28.58	5.333(1)	9.244(2)	10.152(3)	100.164(7)	492.6(2)
Type II xenoliths													
MS3(1)	1*M*	*C*2/*m*	1167	3.20	2.99	0.962	4.06	35.39	5.3402(2)	9.2461(3)	10.1866(3)	100.138(2)	495.12(3)
MS3(2)	1*M*	*C*2/*m*	1080	1.80	2.43	0.980	4.41	34.21	5.3403(1)	9.2485(3)	10.1867(3)	100.132(2)	495.27(2)
MS5	1*M*	*C*2/*m*	582	4.30	2.59	1.003	4.07	27.20	5.3314(3)	9.2290(6)	10.1801(6)	100.051(4)	493.21(5)
MS7	1*M*	*C*2/*m*	588	3.66	2.76	0.909	4.43	27.51	5.3207(1)	9.2099(2)	10.1034(3)	99.959(2)	487.64(2)
MS8(1)	1*M*	*C*2/*m*	586	2.75	2.16	1.036	4.09	27.42	5.3216(4)	9.2114(7)	10.1060(7)	99.949(2)	487.94(6)
MS8(2)	1*M*	*C*2/*m*	579	2.26	2.64	1.073	4.10	27.19	5.3213(2)	9.2034(4)	10.1048(3)	99.954(2)	487.42(3)
MS11	1*M*	*C*2/*m*	583	2.11	1.8	1.113	4.07	27.35	5.3420(1)	9.2461(2)	10.1635(2)	100.219(1)	494.04(2)
Tuffs													
MS10	1*M*	*C*2/*m*	1174	2.36	2.52	1.014	4.07	35.45	5.3408(1)	9.2497(2)	10.1633(3)	100.205(2)	494.13(2)
Lavas													
MS13	1*M*	*C*2/*m*	575	4.15	3.07	1.076	4.07	27.46	5.3399(4)	9.2483(4)	10.1688(7)	100.217(3)	494.22(5)
MS14(1)	$2M_1$	*C*2/*c*	1463	4.43	3.27	0.892	2.04	30.44	5.3341(4)	9.2403(7)	20.085(2)	95.151(2)	986.0(1)
MS14(2)	$2M_1$	*C*2/*c*	2817	3.07	3.37	1.029	4.07	38.71	5.3449(3)	9.2375(5)	20.095(1)	95.143(4)	988.1(1)

TABLE 6A. Relevant cation-anion bond lengths of refined Mt. Sassetto 1*M* micas

Rock type	Ignimbrite	Type I xenoliths		Type II xenoliths							Tuff	Lava
Sample	MS2	MS9	MS12	MS3(1)	MS3(2)	MS5	MS7	MS8(1)	MS8(2)	MS11	MS10	MS13
Tetrahedron												
T-O1	1.652(1)	1.654(1)	1.650(2)	1.653(1)	1.6567(8)	1.658(2)	1.648(2)	1.651(2)	1.650(2)	1.653(1)	1.6521(9)	1.649(2)
T-O1′	1.650(1)	1.658(1)	1.652(2)	1.657(1)	1.6567(9)	1.659(2)	1.646(2)	1.647(2)	1.647(2)	1.653(1)	1.654(1)	1.655(2)
T-O2	1.6508(7)	1.6551(8)	1.6511(9)	1.6551(7)	1.6560(5)	1.656(1)	1.649(1)	1.6483(9)	1.6468(9)	1.6523(6)	1.6533(5)	1.652(1)
T-O3	1.664(1)	1.670(1)	1.668(2)	1.666(1)	1.670(1)	1.669(2)	1.686(2)	1.684(2)	1.683(2)	1.667(1)	1.668(1)	1.666(2)
⟨T-O⟩	1.654	1.659	1.655	1.658	1.660	1.661	1.657	1.658	1.657	1.656	1.657	1.656
Octahedron (M1)												
M1-O3 (×4)	2.109(1)	2.100(1)	2.108(2)	2.105(1)	2.1034(8)	2.098(2)	2.099(2)	2.095(1)	2.098(1)	2.1095(9)	2.1103(8)	2.109(2)
M1-O4 (×2)	2.054(2)	2.042(2)	2.046(2)	2.054(2)	2.053(1)	2.044(3)	2.001(3)	2.001(2)	2.006(2)	2.057(1)	2.055(1)	2.059(3)
⟨M1-O⟩	2.091	2.081	2.087	2.088	2.087	2.080	2.066	2.064	2.067	2.092	2.092	2.092
Octahedron (M2)												
M2-O3 (×2)	2.085(1)	2.087(1)	2.081(2)	2.088(1)	2.0855(9)	2.086(2)	2.090(2)	2.093(2)	2.091(2)	2.086(1)	2.0858(9)	2.086(2)
M2-O3′ (×2)	2.113(1)	2.109(1)	2.117(1)	2.110(1)	2.1088(8)	2.107(2)	2.129(2)	2.134(1)	2.128(1)	2.116(1)	2.1169(8)	2.113(2)
M2-O4 (×2)	2.001(1)	2.005(1)	1.995(1)	2.016(1)	2.0119(8)	2.009(2)	1.946(2)	1.946(1)	1.949(1)	2.000(1)	2.0015(8)	2.007(2)
⟨M2-O⟩	2.066	2.067	2.064	2.071	2.069	2.067	2.056	2.058	2.053	2.067	2.068	2.067
Interlayer cation												
A-O1 (×4)	3.022(1)	2.963(1)	3.014(2)	2.994(1)	2.9853(9)	2.949(2)	2.953(2)	2.953(2)	2.950(2)	3.012(1)	3.011(1)	3.022(2)
A-O2 (×2)	3.018(2)	2.970(2)	3.016(2)	2.995(2)	2.989(1)	2.957(3)	2.964(3)	2.962(2)	2.962(2)	3.014(2)	3.012(1)	3.025(3)
A-O1′ (×4)	3.267(1)	3.341(2)	3.268(2)	3.311(1)	3.319(1)	3.353(2)	3.296(2)	3.298(2)	3.295(2)	3.276(1)	3.277(1)	3.271(2)
A-O2′ (×2)	3.291(2)	3.358(2)	3.288(2)	3.327(2)	3.334(1)	3.367(3)	3.313(3)	3.322(2)	3.319(2)	3.297(2)	3.297(1)	3.288(3)
$\langle A\text{-}O\rangle_{inner}$	3.021	2.965	3.015	2.994	2.987	2.952	2.957	2.956	2.953	3.013	3.011	3.023
$\langle A\text{-}O\rangle_{outer}$	3.275	3.347	3.275	3.316	3.324	3.358	3.302	3.306	3.304	3.283	3.284	3.277

by phenocrysts of plagioclase, sanidine, biotite, ortho- and clinopyroxene, and subordinate quartz. Devitrified glass in the groundmass, grayish to yellowish-brown in color, shows low transparency. Sanidine, plagioclase, and subordinate ilmenite, rutile, apatite, and zircon are present in the groundmass as microlites. The presence of secondary mineral species, such as smectite and Fe-hydroxides, was revealed during SEM-EDS observations, and confirmed via Gandolfi X-ray analysis.

Lavas, mainly vitrophyric in texture (Fig. 2b), show the same assemblage as tuffs, ignimbrites, and Type I xenoliths. Also in this case, primary glass in the groundmass is nearly absent due to devitrification. A doleritic texture is common in Type II xenoliths (Fig. 2c), showing plagioclase, sanidine, biotite (euhedral), clino- and orthopyroxene (subhedral) as major phases, and ilmenite, apatite, titanomagnetite, and quartz as minor ones.

The trioctahedral mica crystals from Mt. Sassetto can be divided into two main groups, according to their euhedral vs. anhedral habit. Euhedral crystals, present only in Type II xenoliths (MS3, MS5, MS7, MS8, MS11, and MS15), are up to 300 μm long and 50 μm thick, and all show brown to pale-greenish-brown pleochroism, with the exception of micas from samples MS7 and MS8, which are reddish brown. Anhedral mica crystals occur in tuffs and ignimbrites (MS1, MS2, MS4, and MS10), in lavas (MS13 and MS14), and in Type I xenoliths (MS9 and MS12). They all show similar petrographic features, being up to 1 mm long and 0.5 mm thick, pleochroism from brown to pale greenish brown, a commonly deformed shape and corroded rims.

Whole-rock composition

Major-and-trace element contents are reported in Table 2[1]. According to the Irvine and Baragar (1971) classification, all Type II xenoliths but MS5 are alkaline, whereas the other studied

TABLE 6B. Relevant cation-anion bond lengths of refined Mt. Sassetto $2M_1$ micas

Rock type	Ignimbrite		Lavas	
Sample	MS1	MS4	MS14(1)	MS14(2)
Tetrahedron (T1)				
T1-O11	1.652(2)	1.651(2)	1.654(2)	1.653(1)
T1-O21	1.651(2)	1.652(2)	1.649(2)	1.655(1)
T1-O22	1.649(2)	1.656(2)	1.654(2)	1.651(1)
T1-O31	1.668(2)	1.669(2)	1.664(2)	1.665(1)
⟨T1-O⟩	1.655	1.657	1.655	1.656
Tetrahedron (T2)				
T2-O11	1.649(2)	1.654(2)	1.647(2)	1.653(1)
T2-O21	1.649(2)	1.650(2)	1.651(2)	1.651(1)
T2-O22	1.650(2)	1.647(2)	1.644(2)	1.651(1)
T2-O32	1.665(2)	1.662(2)	1.660(2)	1.664(1)
⟨T2-O⟩	1.653	1.653	1.651	1.655
Octahedron (M1)				
M1-O31 (×2)	2.109(2)	2.110(2)	2.108(2)	2.113(1)
M1-O32 (×2)	2.109(2)	2.115(2)	2.114(3)	2.113(1)
M1-O4 (×2)	2.051(2)	2.046(2)	2.053(3)	2.053(1)
⟨M1-O⟩	2.090	2.090	2.092	2.093
Octahedron (M2)				
M2-O31	2.081(2)	2.078(2)	2.080(3)	2.083(1)
M2-O31′	2.116(2)	2.120(2)	2.118(3)	2.118(1)
M2-O32	2.081(2)	2.082(2)	2.082(3)	2.084(1)
M2-O32′	2.117(2)	2.121(2)	2.120(2)	2.118(1)
M2-O4	1.995(2)	1.992(2)	1.997(2)	1.998(1)
M2-O4′	1.995(2)	1.993(2)	2.005(3)	2.001(1)
⟨M2-O⟩	2.065	2.064	2.067	2.067
Interlayer cation				
A-O11 (×2)	3.016(2)	3.015(2)	3.020(2)	3.020(1)
A-O11′ (×2)	3.289(2)	3.289(2)	3.291(2)	3.289(1)
A-O21 (×2)	3.012(2)	3.016(2)	3.017(2)	3.018(1)
A-O21′ (×2)	3.270(2)	3.267(2)	3.270(3)	3.268(1)
A-O22 (×2)	3.012(2)	3.018(2)	3.021(2)	3.021(1)
A-O22′ (×2)	3.271(2)	3.266(2)	3.272(2)	3.274(1)
$\langle A\text{-}O\rangle_{inner}$	3.013	3.016	3.019	3.020
$\langle A\text{-}O\rangle_{outer}$	3.277	3.276	3.278	3.277

samples are subalkaline (Fig. 3). Following TAS classification (Le Bas et al. 1992), the MS1 ignimbrite is an andesite lying at the boundary with the trachyandesite field. The other two ignimbrite (MS2 and MS4) and lava samples are trachydacites. Type I xenolith MS12 is an andesite, and, in terms of total alkali and SiO_2 content, it is very similar to ignimbrites MS2 and MS4. Type II xenolith MS5 is a basalt lying at the boundary with basaltic-andesite, whereas MS11 is a basaltic-trachyandesite. MS7 and MS8 are basaltic-trachyandesites lying next to the boundary with the trachyandesite field and, finally, MS3 is a trachyandesite. Whole-rock data from De Rita et al. (1997), reported in Figure 3 for comparison, are consistent with the data presented here.

Type II xenoliths MS7 and MS8 contain the highest amounts of the light rare-earth elements (LREE) and Y. The LREE and Y contents of other Type II xenoliths, Type I xenoliths, ignimbrites, and lavas are much lower and not significantly variable. Samples MS7 and MS8 are also the highest in Zr and Sr. Type II xenolith MS3 is the richest in Ba. Type II xenoliths MS11, MS3, and MS5 show significant S, Ni, Cr, Zn, and Cu contents, thus suggesting the occurrence of trace mineral phases such as sulfides and/or heavy metal hydroxides.

Mica chemistry

The mica crystals from Mt. Sassetto range in composition from ferroan phlogopite to magnesian annite (Fig. 4a, Table 3[1]). The mean value of $Mg/(Mg + Fe_{tot})$, X_{Mg}) is nearly constant in micas from tuffs, lava domes, and ignimbrites. Variable $Mg/(Mg + Fe_{tot})$ values characterize micas from Type I and Type II xenoliths.

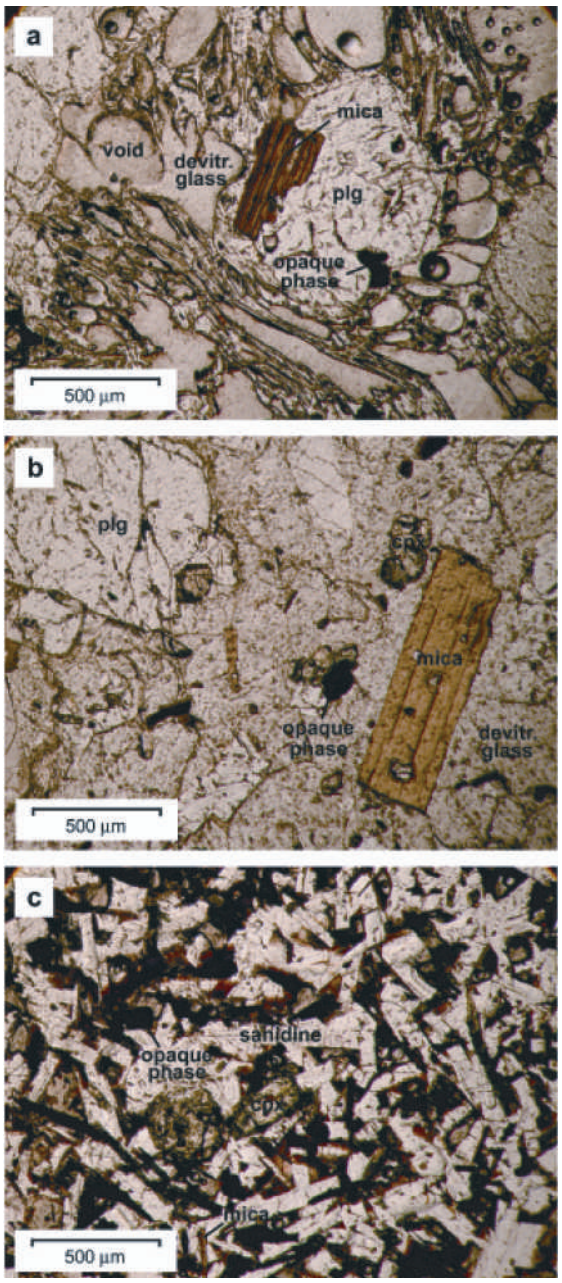

FIGURE 2. Photomicrographs of the three different textures recognized in the Mt. Sassetto volcanic rocks: (**a**) vitrophyric pseudofluidal (ignimbrite sample MS2, plane-polarized light); (**b**) vitrophyric (lava sample MS13, plane-polarized light); (**c**) doleritic (Type II xenolith MS8, plane-polarized light). Thickness of the thin section = 40 µm.

Tetrahedral Al content ranges from 1.165 to 1.320 apfu. The total Al content ($^{[IV]}Al + {}^{[VI]}Al$) mean is the highest in micas from Type I and Type II xenoliths. The Ti content ranges from 0.121 to 0.321 apfu; it is highly variable in micas from xenoliths, where it covers the full range.

Potassium content ranges from 0.860 to 0.933 apfu, and the Na content is restricted in range and low (values similar in all

TABLE 7. Selected geometrical parameters obtained from structure refinements of Mt. Sassetto micas

Rock type	Ignimbrite			Type I xenoliths		Type II xenoliths							Tuff	Lavas		
Polytype	$2M_1$	1*M*	$2M_1$	1*M*	1*M*	1*M*	1*M*	1*M*	1*M*	1*M*	1*M*	1*M*	1*M*	1*M*	$2M_1$	$2M_1$
Sample	MS1	MS2	MS4	MS9	MS12	MS3(1)	MS3(2)	MS5	MS7	MS8(1)	MS8(2)	MS11	MS10	MS13	MS14(1)	MS14(2)
Parameters describing the tetrahedron																
α (°)	5.75	5.57	5.65	8.35	5.69	7.03	7.38	8.88	7.52	7.65	7.62	5.89	5.94	5.55	5.66	5.62
Δz (Å)	0.028	0.018	0.028	0.019	0.028	0.014	0.017	0.019	0.025	0.029	0.030	0.019	0.019	0.018	0.028	0.028
⟨O-O⟩$_{basal}$ (T1) (Å)	2.682	2.681	2.683	2.693	2.681	2.690	2.692	2.697	2.683	2.684	2.683	2.684	2.685	2.682	2.684	2.684
⟨O-O⟩$_{basal}$ (T2) (Å)	2.678		2.678					2.677	2.681							
τ(T1) (°)	110.27	110.32	110.40	110.09	110.45	110.22	110.20	110.01	109.94	109.96	109.99	110.35	110.35	110.35	110.24	110.36
τ(T2) (°)	110.35		110.44					110.23	110.38							
THA*	36.83	36.88	36.85	36.63	36.85	36.85	36.84	36.61	36.54	36.55	36.52	36.92	36.92	36.92	36.85	36.91
Parameters describing the octahedra																
ψM1 (°)	59.38	59.34	59.39	59.22	59.42	59.18	59.31	59.22	59.69	59.62	59.59	59.35	59.33	59.29	59.27	59.34
ψM2 (°)	58.97	58.94	58.97	58.99	59.05	58.90	59.01	59.01	59.50	59.52	59.42	58.95	58.94	58.90	58.86	58.91
Off center shift M2	0.059	0.052	0.062	0.053	0.059	0.041	0.040	0.044	0.108	0.111	0.105	0.055	0.056	0.051	0.056	0.055
ΔM (Å)	0.025	0.024	0.026	0.014	0.023	0.017	0.018	0.013	0.012	0.006	0.011	0.024	0.024	0.024	0.024	0.026
Octahedral-interlayer parameters																
A-O4	3.990(2)	3.992(1)	3.999(2)	4.007(2)	3.994(2)	3.998(1)	4.005(1)	4.004(2)	4.012(2)	4.011(2)	4.007(2)	3.993(1)	3.991(1)	3.986(2)	3.989(2)	3.997(2)
A-O4$_{(001)}$	0.351(2)	0.698(1)	0.351(2)	0.711(2)	0.703(2)	0.703(1)	0.702(1)	0.709(2)	0.737(2)	0.739(2)	0.735(2)	0.697(1)	0.700(2)	0.696(2)	0.345(2)	0.350(2)
Sheet thickness																
Tetrahedral (Å)	2.268	2.260	2.273	2.259	2.265	2.260	2.265	2.258	2.279	2.276	2.275	2.264	2.264	2.260	2.261	2.27
Octahedral (Å)	2.128	2.132	2.129	2.130	2.123	2.140	2.130	2.129	2.086	2.087	2.093	2.132	2.134	2.137	2.138	2.135
Interlayer separation (Å)	3.330	3.348	3.329	3.387	3.339	3.368	3.368	3.379	3.307	3.315	3.310	3.342	3.340	3.351	3.342	3.333

Notes: α (tetrahedral rotation angle) = $\Sigma_{i=1}^{6}\alpha_i/6$ where $\alpha_i = |120° - \varphi_i|/2$ and where φ_i is the angle between basal edges of neighboring tetrahedra articulated in the ring; $\Delta z = [z_{(O_{basal})}\max - z_{(O_{basal})}\min]\ [\csin\beta]$;

τ (tetrahedral flattening angle) = $\sum_{i=1}^{3}(O_{basal} - \hat{T} - O_{basal})i / 3$;

THA (Tetrahedral Hexagon Area) = area of the hexagon defined by tetrahedral basal oxygen edges; ψ (octahedral flattening angle) = $\cos^{-1}$[octahedral thickness/(2<M-O>)] (Donnay et al. 1964);

$$A\text{-}O4_{(001)} = \sqrt{\left|\overrightarrow{A\text{-}O4}\right|^2 - \left|(\overrightarrow{A\text{-}O4})\mathbf{c}^*\right|^2}$$

M2 off-center shift is the distance between M2 cation and ($X_{c,M2}$, $Y_{c,M2}$, $Z_{c,M2}$).

Where: $X_{c,M2} = \frac{1}{6}\left(\sum_{i=1}^{6} X_{o,i}\right)$; $Y_{c,M2} = \frac{1}{6}\left(\sum_{i=1}^{6} Y_{o,i}\right)$; $Z_{c,M2} = \frac{1}{6}\left(\sum_{i=1}^{6} Z_{o,i}\right)$;

and the terms $X_{o,i}$, $Y_{o,i}$, $Z_{o,i}$ are a generic O atom defining M2 coordination.

* Tetrahedral Hexagon Area.

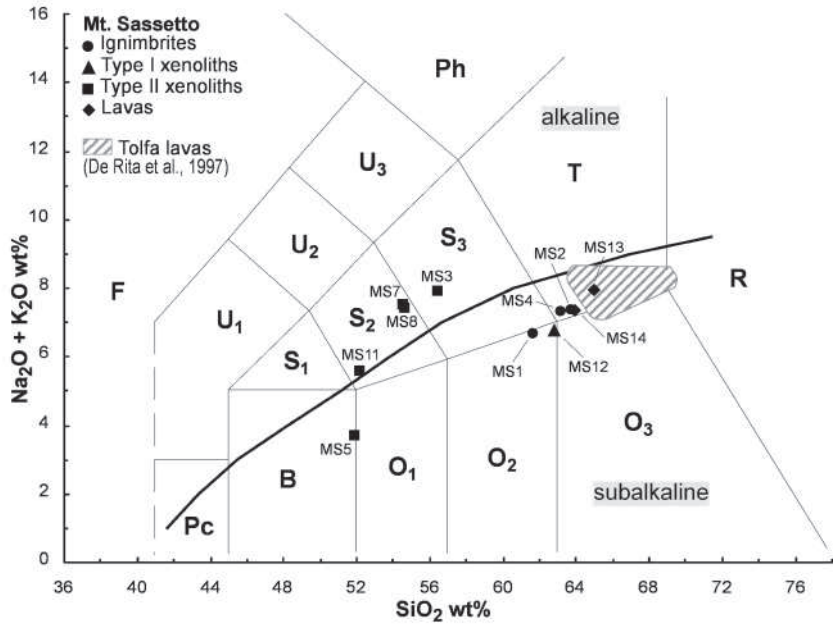

FIGURE 3. Classification of volcanic rocks from Mt. Sassetto after Irvine and Baragar (1971) and Le Bas et al. (1992). Rock samples from Mt. Sassetto analyzed by De Rita et al. (1997) are reported for comparison (dashed gray field). F = Foidite; U_1 = Basanite and Tephrite; U_2 = Phonotephrite; U_3 = Tephriphonolite; Ph = Phonolite; Pc = Picrite; B = Basalt; O_1 = Basaltic-andesite; O_2 = Andesite; O_3 = Dacite; *R* = Rhyolite; T = Trachyte and Trachydacite; S_2 = Basaltic-trachyandesite; S_3 = Trachyandesite.

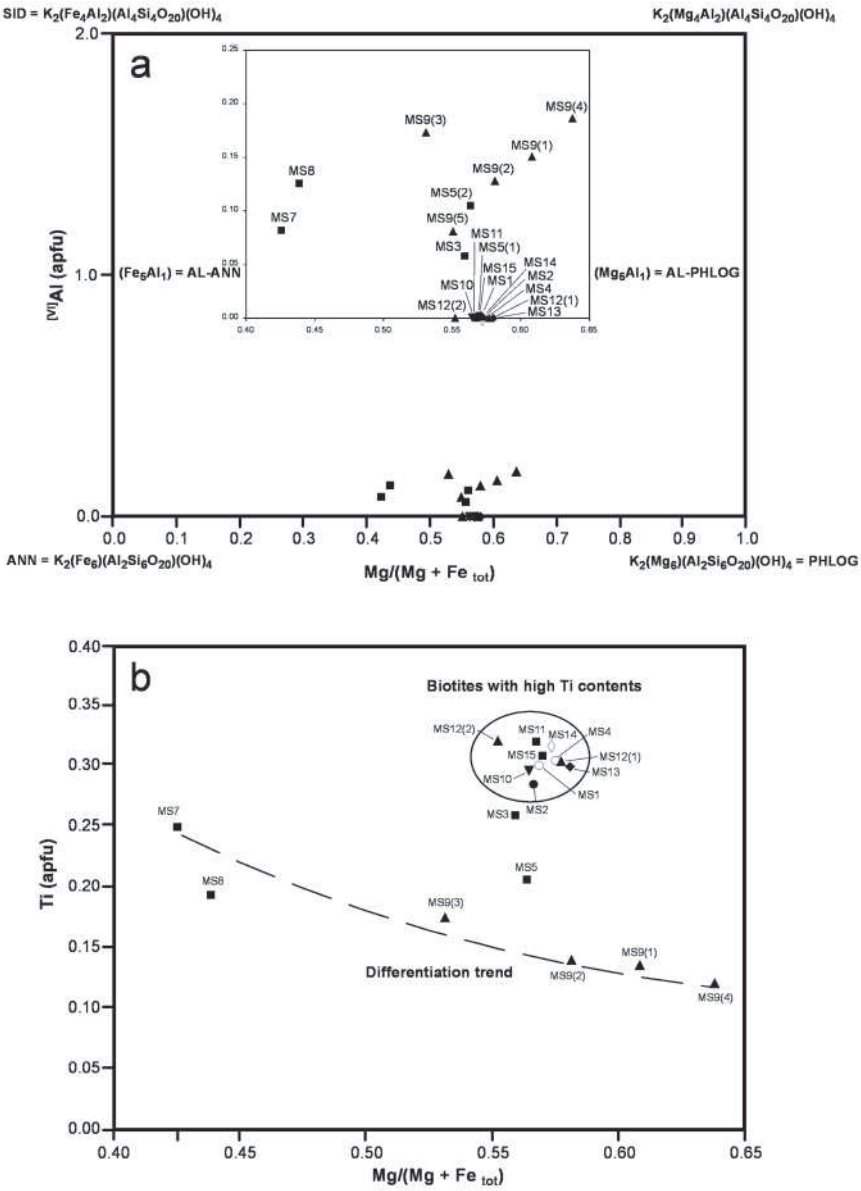

FIGURE 4. Micas from Mt. Sassetto: (**a**) classification diagram after Guidotti (1984); (**b**) Mg/(Mg + Fe_{tot}) vs. Ti (wt%) plot. Symbols: circle = micas from ignimbrites; triangle up = micas from Type I xenoliths; square = micas from Type II xenoliths; triangle down = micas from tuffs; diamond = micas from lavas; filled symbols = 1*M* polytype crystals; open symbols = $2M_1$ polytype crystals.

the samples, around 0.06 apfu), but always present as a substituent for K in the interlayer site. Euhedral crystals from Type II xenoliths show the highest Ba content. Fluorine content ranges from 0.147 to 0.469 apfu. The greatest fluorine variability occurs in micas from Type I xenoliths, where the full variation range for this element is covered. Finally, micas from Type I xenolith MS9 are peculiar in that they show a significant compositional variability ($0.121 \le Ti \le 0.175$ apfu; $0.532 \le Mg/(Mg + Fe_{tot}) \le 0.638$); $0.128 \le {}^{VI}Al \le 0.187$ apfu).

Crystal structure and crystal chemistry of micas

MS1, MS4, and MS14 mica samples present a $2M_1$ sequence, whereas all the other belong to 1*M* polytype. This latter polytype dominates in Type I, Type II xenoliths, and in *cinerites* (tuff matrix), whereas the 1*M* and $2M_1$ polytypes coexist in ignimbrites and lavas. Some authors (e.g., Baronnet 1980; Kogure 2002) relate different polytypic sequences in micas either to genetic conditions or to secondary crystallization effects. However, the absence of adequate data on the polytypes from the Mt. Sassetto area prevents a firm conclusion on this point.

1*M* mica samples MS7, MS8(1), and MS8(2) have unit-cell parameters (Fig. 5) that are significantly smaller than other samples from Mt. Sassetto, and among the lowest refined for the phlogopite–annite join micas (Brigatti and Guggenheim 2002; Cruciani and Zanazzi 1994). These micas can also show an appreciable M1 and M2 site inequality. This feature is common, and also evident, in other micas from Mt. Sassetto, where it is always associated with an increase in Ti content (Table 4). These crystal-chemical features, together with the high Fe-total content and the low Ti content, if compared with samples reported by Cruciani

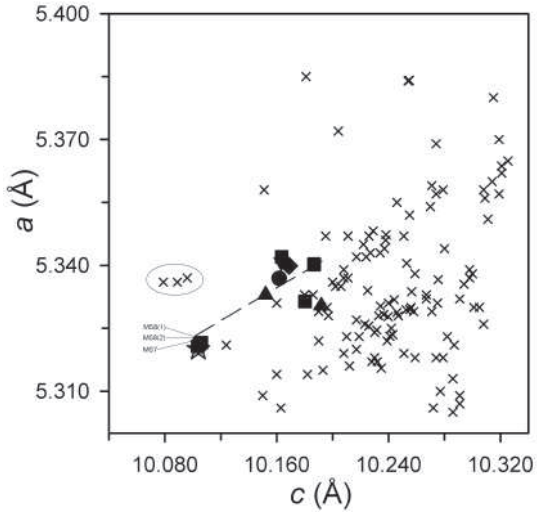

FIGURE 5. Micas from Mt. Sassetto: *a* vs. *c* plot. Symbols for studied samples as in Figure 4; crosses = igneous micas from literature (Baschieri 2005; Brigatti and Guggenheim 2002; Brigatti et al. 2005; Cruciani and Zanazzi 1994; Schingaro et al. 2001); gray star = Pines Peak "oxybiotite" (Ohta et al. 1982). Circled samples from the literature refer to samples 21, 22, and 23 of Cruciani and Zanazzi (1994). Error bars are minor than symbol dimensions.

and Zanazzi (1994) (i.e., samples no. 21, 22, and 23 showing *c* unit-cell parameter values of 10.089, 10.079, and 10.096 Å, respectively, and Ti contents of 0.607, 0.650, and 0.592, respectively; circled in Fig. 5), suggest that, at least in part, Fe is in the oxidized form. A further confirmation comes from the refined mean electron counts and mean octahedral bond lengths, which suggest Fe^{3+}/Fe_{total} ratios of 0.529, 0.511, and 0.516 for MS7, MS8(1), and MS8(2) mica samples, respectively. These values are compatible with Fe^{3+} being dominant in the M2 sites and Fe^{2+}, Mg, or vacancies in the M1 sites (Tables 6a and 9[1]). Due to the small size of the samples and to the limited material available, a cross-check with other experimental techniques was not possible. An evaluation, based on data from the literature (Rancourt et al. 2001; Redhammer et al. 2005), qualitatively confirms the Fe^{3+} values indicated by crystal chemistry. Further crystal-chemical confirmations are provided, for samples under analysis, by oxy-substitution, where interlayer separation decreases both as a function of Ti and of Fe^{3+}, and by a remarkable number of octahedral vacancies (0.208–0.243 positions per formula unit) in Fe^{3+}-rich samples.

All other samples from Mt. Sassetto, both the 1*M* and $2M_1$ polytypes, are significantly affected by the octahedral Ti substitution. In particular, an increase in Ti is accompanied by a decrease in Fe^{2+} and octahedral Al^{3+} (Table 4). Furthermore, the overall octahedral charge increases with Ti together with the anionic charge, thus suggesting a Ti-oxy substitution mechanism. Some crystals present octahedral vacancies, hence the two main vectors regulating Ti entry into the mica structure appear to be the Ti-oxy $[^{VI}Ti^{4+VI}(Mg,Fe)^{2+}_{-1}(OH)^{-}_{-2}O^{2-}_{2}]$ and Ti-vacancy $[^{VI}Ti^{4+VI}\square^{VI}(Mg,Fe)^{2+}_{-2}]$. The positive Si vs. Ti correlation negates Ti-Tschermak substitution. Several geometric parameters such as the interlayer cation -O4 bond distance (A-O4), the octahedral anionic site displacement from the interlayer cation along (001) [$A\text{-}O4_{(001)}$, correlation coefficient $R = 0.925$], and the interlayer separation ($R = 0.928$) decrease with Ti increasing (Figs. 6a and 6b; Tables 4 and 7). This trend is consistent with the deprotonation of the O4 anionic position, and thus with a lower repulsion between the O4 anion and A cation in the interlayer. The increase of the monoclinic angle β with Ti ($R = 0.931$) and the related decrease in overall shift ($R = 0.902$) further confirm the influence of Ti content on interlayer topology. Also, the decrease of tetrahedral rotation angle α with Ti ($R = 0.911$) can be related to Ti-oxy substitution mechanism (Fig. 6c). α is linked to an increase in the area delimited by the six tetrahedral basal oxygen atoms, i.e., the Tetrahedral Hexagon Area (THA, Table 7) (Ti vs. THA, $R = 0.955$), which also defines the cavity hosting the interlayer cation. This feature is related to the impinging of the interlayer cation inside this latter cavity, which in turn needs to enlarge laterally. The tetrahedral flattening angle τ (Table 7) also increases with Ti ($R = 0.900$). This effect can also be related to interlayer interactions (Brigatti and Guggenheim 2002).

Titanium content significantly affects most octahedral parameters as well. In particular, the O3-O4 edge of the M1 octahedron ($R = 0.964$) and ⟨M1-O⟩ ($R = 0.936$) increase with Ti (Fig. 6d; Tables 4 and 6a). The topology of the M2 site is less markedly affected by Ti substitution, despite the fact that Ti is usually assumed to be located in M2, in line with the basic principle according to which, in trioctahedral micas, the topology of M1 is more sensitive to octahedral substitutions than the topology of M2 (Brigatti et al. 2003).

The micas showing the $2M_1$ polytype present crystal-chemical features not significantly different from the Fe^{3+}-free 1*M* polytype samples. The average Ti content is greater in $2M_1$ micas than in the 1*M* ones, and thus structural variations associated with Ti-oxy substitution are also enhanced (Figs. 6a–6d). To quote an example, interlayer separation is, on average, smaller in $2M_1$ micas than in the 1*M* ones (Fig. 6b).

The three Fe^{3+}-rich samples mentioned above show the smallest unit-cell parameters. In particular, their *c* cell parameters are significantly smaller than in other micas (Table 5). Like in oxybiotite (Ohta et al. 1982) and in some Ti-rich micas (Cruciani and Zanazzi 1994), the out-of-center shift of the M2 cation, usually negatively correlated to *c*, is the greatest (Table 7). This effect, which may be related to a decrease in interlayer separation and octahedral thickness, is usually associated with Ti substitution (Cruciani and Zanazzi 1994). Our data qualitatively confirm these crystal-chemical trends also for Fe^{3+} substitution, even if with a much greater intensity, as also testified by the extreme values of these structural parameters in Fe^{3+}-rich samples, also including oxy-biotite (Ohta et al. 1982). These features agree well with an octahedral charge that is the highest in the considered data set, and with a tetrahedral charge that is among the lowest, following an increased Al for Si tetrahedral substitution and thus, unlike Ti-rich samples, suggesting a Tschermak substitution. Those samples also show a greater number of octahedral vacancies (up to 0.24 apfu) and, unlike most trioctahedral micas, mean electron counts for M2 greater than for M1, probably due to the presence of the octahedral vacancies themselves. Vacancies also account for a greater distortion of the octahedral sites. The ψ angle values for M1 and M2 (Table 7) are the largest in the considered data set. The distortion is also evidenced by the great

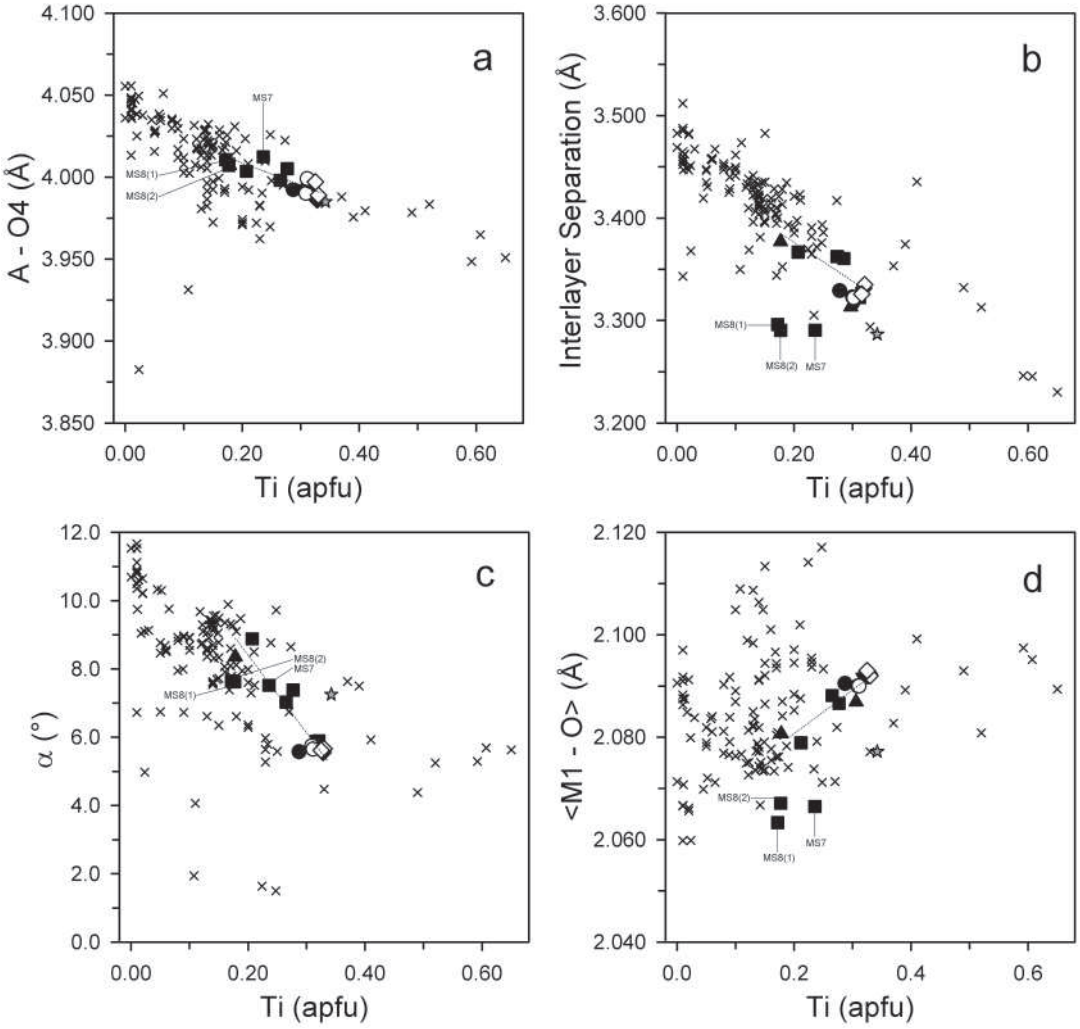

FIGURE 6. Micas from Mt. Sassetto: variation of structural parameters vs. Ti (apfu). (**a**) Distance between the interlayer cation and the octahedral anionic position (A-O4) Vs. Ti; (**b**) Interlayer separation vs. Ti; (**c**) tetrahedral rotation angle α vs. Ti; (**d**) mean ⟨M1-O⟩ distance vs. Ti. Symbols as in Figure 4; symbols for literature data as in Figure 5. Linear regressions reported in each plot are calculated on the basis of 1*M* Fe^{3+}-free mica samples only, thus excluding samples MS7, MS8(1), and MS8(2); for their respective *R* values see the text. Error bars for structural parameters are minor than symbol highness.

differences existing in the octahedral distances: thus, M2-O3 distances are among the greatest, whereas M1-O4 and M2-O4 distances are among the smallest. The displacement of the O4 anion from the interlayer cation on the (001) plane is also the greatest in Fe^{3+}-rich samples, confirming that these crystals are also affected by oxy-substitution, as evidenced by their low interlayer separation. Thus, it appears that their Fe^{3+} contents can be compensated combining the following exchange mechanisms: $^{VI}Fe^{2+}_{-3}{}^{VI}Fe^{3+}_{2}{}^{VI}\square$, $^{VI}Fe^{2+}_{-1}{}^{VI}Fe^{3+}(OH)^{-}_{-1}O^{2-}$ and, $^{VI}Fe^{2+}_{-1}{}^{VI}Fe^{3+}{}^{IV}Si_{-1}{}^{IV}Al^{3+}$ (Rancourt et al. 2001; Redhammer et al. 2005). The "oxybiotite" from Ruiz Peak (Ohta et al. 1982) is the trioctahedral mica with the greatest octahedral Fe^{3+} content described so far, where the Fe^{3+}-oxy-substitution is predominant. Actually, this mica is richer in Fe^{3+} than all samples from Mt. Sassetto, and thus its interlayer separation is smaller. The Ruiz Peak "oxybiotite" unit-cell parameters *a*, *b*, and *c* are close to the values found in samples MS7, MS8(1), and MS8(2) from Mt. Sassetto. However, the Ruiz Peak "oxybiotite" shows no evidence of octahedral vacancies, and its tetrahedral charge is appreciably greater than in Fe^{3+}-rich samples from Mt. Sassetto.

A detailed description of the crystal-chemical mechanisms associated with Fe oxidation in annite was provided by Rancourt et al. (2001) and by Virgo and Popp (2000). In particular, when a synthetic annite is progressively heated in air, two distinct oxidation mechanisms are observed: (1) Fe^{3+}-oxy substitution, which occurs at $T \leq 350$ °C, and (2) Fe^{3+}-vacancy substitution, which occurs at $T > 350$ °C. However, both oxidation mechanisms are subjected to crystal-chemical constraints. The Fe^{3+}-vacancy mechanism induces a variation in the lateral dimensions of the mica layer introducing octahedral vacancies and thus increasing the size difference between the two octahedral M1 and M2 sites. The Fe^{3+}-oxy mechanism can be of limited extent when F atoms are present in the O4 anionic positions. Moreover, both mechanisms are also controlled by f_{H_2}. An increase in f_{H_2} shifts the

equilibrium of Fe^{3+}-oxy reaction toward the left side. In contrast, a decrease in f_{H_2} promotes a greater Fe oxidation, thus shifting the reaction to the right side. The Fe^{3+}-Tschermak substitution can point out complex ion-exchange reactions, implying either a diffusion of chemical elements inward to the mica layer or a liquid-to-solid interface reaction. Results suggest that the presence of different exchange mechanisms introducing Fe^{3+} in the Mt. Sassetto micas reflect a complex petrogenetic environment.

Petrologic implications

The previously reported mica data may contribute to the description of magma evolution processes operating during the emplacement of the eruptive sequence in Mt. Sassetto.

In the Ti vs. $Mg/(Mg + Fe_{tot})$ diagram plotted in Figure 4b, ferroan phlogopites from xenoliths MS9 (Type I), MS7, and MS8 (Type II) define a negative correlation extending from the most restitic micas MS9(4), ideally in equilibrium with a more-primitive magma composition, to micas MS7, ideally in equilibrium with a more-evolved melt enriched in Fe and Ti. Such a differentiation trend could result from small-scale, fractional crystallization processes taking place in the magma chamber (or in a more-complex feeding system beneath the eruptive apparatus). Fractionation of mica itself, among the other femic phases, could have contributed to this chemical differentiation.

A progressive deviation from this trend characterizes micas from MS5, MS3 (Type II), and all the other micas from Type I, Type II xenoliths, ignimbrites, tuffs, and lavas. These samples show $Mg/(Mg + Fe_{tot})$ ratios around 0.56 and high Ti contents. This deviation can be ascribed neither to fractional crystallization nor to mixing mechanisms, but rather to a variation in intensive parameters (T, P, f_{H_2}, f_{O_2}, f_{H_2O}). At a given melt composition, this variation can promote Ti re-partitioning in micas either to accomplish charge balance and topologic constraints, or because of the disappearance of a Ti-competing phase.

Compositional variations, similar to the ones observed for micas from Mt. Sassetto, are widely described in the literature for amphiboles from igneous environments. Experimental data on these latter phases can contribute toward explaining some relationships between crystal-chemical and environmental factors. Increasing pressure results in higher ^{VI}Al and lower ^{VI}Ti contents in amphiboles, as derived from sub- and super-solidus experiments (Oba et al. 1986; Ernst and Liu 1998; Adam and Green 1994; Fujinawa and Green 1997), whereas high temperatures (>950 °C) favor ^{VI}Al-Ti rich compositions (Allen and Boettcher 1978; Wallace and Green 1991). Thus, if experimental results concerning natural and synthetic amphiboles can be applied to micas, then high Ti contents in these micas are predictive of low-pressure, high-temperature, low f_{H_2}, and moderate to low f_{O_2} conditions (Aoki 1963; King et al. 1999; Miyagi et al. 1998).

The prevailing mechanism introducing Ti in Mt. Sassetto Fe^{3+}-free micas is the Ti-oxy substitution. As suggested by Feeley and Sharp (1996), the H_2 released from the mica structure can react with the O_2 present in the melt, thus increasing its volatile content. This mechanism could represent a further feature controlling the explosivity of eruptions (Virgo and Popp 2000) and could be triggered by the temperature increase observed in the magmatic chamber before an eruption, due to the influx of a new batch of mafic magma (Sparks et al. 1977; Pallister et al. 1992). However, many other environmental factors, such as ascent rate, cooling rate, and grain attributes (inclusions and fracture density), can play a central role.

Indications about the high f_{O_2} conditions of crystallization for MS7 and MS8 (type II xenoliths) can be hypothesized from experimental studies on micas synthesized under controlled oxygen fugacity conditions (Wones and Eugster 1965, Redhammer et al. 1995). In the ternary diagram annite (Fe^{2+})-phlogopite (Mg)-"oxyannite" (Fe^{3+}) in which "buffered" mica compositions are reported (Fig. 7), micas MS7, MS8(1), and MS8(2) fall well above the HM (Hematite-Magnetite) buffer, which represents the highest f_{O_2} values found in the crystallization of magmas (Kleiman et al. 1992). Following these indications, if relevant Fe^{3+} contents and consequent structural features of these micas are of primary origin (i.e., acquired during crystallization in the magmatic chamber), then an abrupt variation in f_{O_2} conditions occurred during the evolution of Mt. Sassetto magmatism. Several mechanisms can promote an increase in f_{O_2} in the magma chamber prior to, during, or just after crystallization: (1) ring fractures associated with high-level intrusions may provide a pathway through which magmas are contaminated with atmospheric oxygen (Rowins et al. 1991); (2) dissociation of water into H_2 and O_2, followed by the preferential escape of H_2 gas (Sato and Wright 1966), although this mechanism would be effective only for magmas with $H_2O/FeO \geq 10$ (Candela 1986); (3) hydrothermal events, as in the case of Ruiz Peak fumaroles, that promoted high-temperature oxidation of the emplaced rhyodacitic lavas (Takeda and Ross 1975; Kogure and Nespolo 2001); or (4) assimilation of hydrothermally altered wall-rocks (Hildreth et al. 1984; Grunder 1987; Bacon et al. 1989).

However, our favorite hypothesis about micas from Type II xenoliths MS7 and MS8 is that their oxidation must be ascribed to a post-eruptive hydrothermal event, namely to the high f_{O_2}

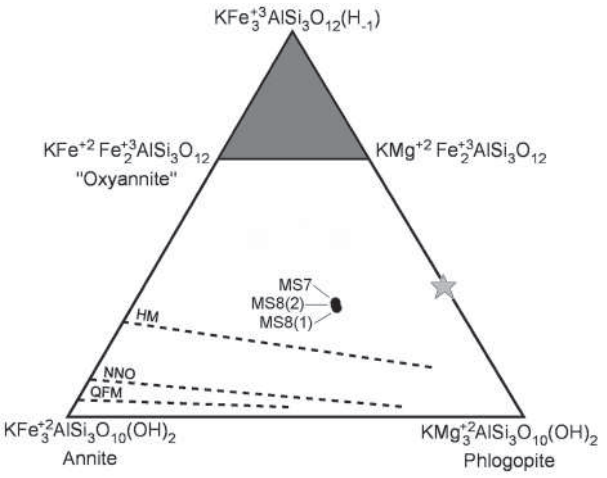

Figure 7. Plot of micas MS7, MS8(1), and MS8(2) from Mt. Sassetto in the ternary system $KFe^{2+}_3AlSi_3O_{10}(OH)_2$-$KMg^{2+}_3AlSi_3O_{10}(OH)_2$-$KFe^{3+}_3AlSi_3O_{12}(H_{-1})$. Star = Pines Peak "oxybiotite" (Ohta et al. 1982). Dashed lines indicate compositions of "buffered" biotites (buffers: HM = Hematite-Magnetite; NNO = Ni-NiO; QFM = Quartz-Fayalite-Magnetite). The gray area represents compositions that are physically impossible to obtain.

and f_{H_2O} values and the moderately high temperatures (≤400 °C, Knight 1977) characterizing an acid-sulfate alteration fluid. Temperature conditions and high Fe mobility in this type of hydrothermal agent are in agreement with the Fe^{3+}-vacancy and Fe^{3+}-Tschermak substitution mechanisms. On the other hand, an Fe-oxy mechanism could provide available H^+ ions, thus regenerating an acid metasomatic agent that is partly neutralized by the interaction with the wall rock. The fact that only micas from MS7 and MS8 xenoliths are highly oxidized could suggest that these latter materials (for which a hypabyssal origin is suggested; cf., Negretti et al. 1966) were collected from deeper regions, more affected by the metasomatic agent, which is expected to decrease in intensity outward. This interpretation is also consistent with crystal-chemical evidence, clearly showing the existence of all the above-mentioned exchange mechanisms. In particular, in Fe^{3+}-rich micas, the M2 site, which shows a greater mean electron count than <M1-O> bond distances and a shorter mean distance, appears to be more affected by oxidation processes and to drive the chemical substitutions affecting the layer, as well as layer topology, since requesting a lower M1 and tetrahedral charge, as well as an increase in anionic negative charge. Unlike Fe^{3+}, Ti substitutions (mostly Ti-oxy) are mostly compensated inside the octahedral sheet, thus hinting to more-limited cation diffusion. Volcanic rocks from Mt. Sassetto include secondary minerals, such as smectite and Fe hydroxides. Their presence is indicative of meteoric alteration processes, which could have affected mica crystal chemistry as well. Atmospheric weathering phenomena can produce non-expanded oxidized biotites with 10 Å periodicity in XRD patterns (Rebertus et al. 1986; Murphy et al. 1998) and with almost all Fe in the trivalent form, not only under tropical wet conditions (Dong et al. 1998), but also under humid-temperate conditions. Jeong and Kim (2003) suggested that, during the saprolitic weathering, the precursor of the transformation "interlaminate biotite-vermiculite → vermiculite → kaolinite + oxides/oxides-hydroxides," is an oxidized and chemically modified biotite, rather than a "fresh" sample. However, it should be noted that altered biotites are characterized by $1M_d$ polytype and not by regular $1M$ sequences. Thus, even if weathering phenomena cannot be excluded, they did not produce the structural modifications usually observed in trioctahedral micas (Baronnet 1980).

The age of Mt. Sassetto volcanic rocks is consistent with an incipient pedogenetic process, and the ubiquitous presence of secondary smectite and Fe hydroxides possibly accounts for it. Nevertheless, it is unlikely that the oxidation of biotites from samples MS7 and MS8 can be related to atmospheric weathering. In fact, temperature conditions associated with this type of alteration process do not match those expected for the observed substitution mechanisms. Moreover, oxidation should affect not only micas from some xenoliths enclosed in pyroclastites, but also micas from the entire wall rock exposed to atmospheric action.

Acknowledgments

We acknowledge precious comments from the two referees P.F. Zanazzi and G. Redhammer and the support from the Associate Editor D. Gatta. Our research on micas enjoys the joint support of Italy's Ministero dell'Istruzione Università e Ricerca (MIUR) and of Università degli Studi di Modena e Reggio Emilia under COFIN 2004 project "Effect of petrological variables on mica crystal chemistry."

References cited

Adam, J. and Green, T.H. (1994) The effects of pressure and temperature on the partitioning of Ti, Sr and REE between amphibole, clinopyroxene and basanitic melts. Chemical Geology, 117, 219–233.

Allen, J.C. and Boettcher, A.L. (1978) Amphiboles in andesite and basalt; II, Stability as a function of P-T-f_{H_2O}-f_{O_2}. American Mineralogist, 63, 1074–1087.

Aoki, K. (1963) The kaersutites and oxykaersutites from alkalic rocks of Japan and surrounding areas. Journal of Petrology, 4, 198–210.

Bacon, C.R., Adami, L.H., and Lanphere, M.A. (1989) Direct evidence for the origin of low $\delta^{18}O$ silicic magmas: Quenched samples of a magma chamber's partially fused granitoid walls, Crater Lake, Oregon. Earth Planetary Sciences Letter, 96, 199–208.

Baronnet, A. (1980) Polytypism in micas: A survey with emphasis on the crystal growth aspects. In E. Kaldis, Ed., Current Topics in Material Science, 5, p. 447–548. North-Holland Publishing Company, Amsterdam.

Baschieri, S. (2005) La cristallografia delle miche nell'interpretazione di eventi vulcanici complessi: il caso del vulcano dei Colli Albani, 112 p. M.S. thesis, Modena and Reggio Emilia University, Italy.

Bertagnini, A., De Rita, D., and Landi, P. (1995) Mafic inclusions in the silica-rich rocks of the Tolfa-Ceriti-Manziana volcanic district (Tuscan Province, Central Italy): chemistry and mineralogy. Mineralogy and Petrology, 54, 261–276.

Brigatti, M.F. and Guggenheim, S. (2002) Mica crystal chemistry and the influence of pressure, temperature, and solid solution on atomistic models. In A. Mottana, F.P. Sassi, J.B. Thompson, Jr., S. Guggenheim, Eds., Micas: Crystal Chemistry and Metamorphic Petrology, 46, p. 1–97. Reviews in Mineralogy and Geochemistry, Mineralogical Society of America, Chantilly, Virginia.

Brigatti, M.F., Guggenheim, S., and Poppi, M. (2003) Crystal chemistry of the $1M$ mica polytype: The octahedral sheet. American Mineralogist, 88, 667–675.

Brigatti, M.F., Caprilli, E., Funiciello, R., Giordano, G., Mottana, A., and Poppi, L. (2005) Crystal chemistry of ferroan phlogopites from the Albano maar lake (Colli Albani volcano, central Italy). European Journal of Mineralogy, 17, 611–621.

Bruker AXS (1999a) SAINT+ (version 6.01). Bruker AXS Inc., Madison, Wisconsin.

——— (1999b) SADABS (version 2.03). Bruker/Siemens area detector absorption and other corrections. Bruker AXS Inc., Madison, Wisconsin.

Candela, P.A. (1986) The evolution of aqueous vapour from silicate melts: effect on oxygen fugacity. Geochimica et Cosmochimica Acta, 50, 1205–1211.

Cesare, B., Cruciani, G., and Russo, U. (2003) Hydrogen deficiency in Ti-rich biotite from anatectic metapelites (El Joyazo, SE Spain): Crystal-chemical aspects and implications for high-temperature petrogenesis. American Mineralogist, 88, 583–595.

Cruciani, G. and Zanazzi, P.F. (1994) Cation partitioning and substitution mechanisms in $1M$ phlogopite: A crystal chemical study. American Mineralogist, 79, 289–301.

De Rita, D., Bertagnini, A., Faccenna, C., Landi, P., Rosa, C., Zarlenga, F., Di Filippo, M., and Carboni, G. (1997) Evoluzione geopetrografica-strutturale dell'area Tolfetana. Bollettino della Società Geologica Italiana, 116, 143–175.

Dong, H., Peacor, D.R., and Murphy, S.F. (1998) TEM study of progressive alteration of igneous biotite to kaolinite throughout a weathered soil profile. Geochimica et Cosmochimica Acta, 62, 1881–1888.

Donnay, G., Morimoto, N., Takeda, H., and Donnay, J.D.H. (1964) Trioctahedral one-layer micas. 1. Crystal structure of a synthetic iron mica. Acta Crystallographica, 17, 1369–1373.

Donovan, J.J. (1995) PROBE: PC-based data acquisition and processing for electron microprobes. Advanced MicroBeam, Inc., Vienna, Ohio.

Ernst, W.G. and Liu, J. (1998) Experimental phase-equilibrium study of Al- and Ti-contents of calcic anphibole in MORB—a semiquantitative thermobarometer. American Mineralogist, 83, 952–969.

Feeley, T.C. and Sharp, Z.D. (1996) Chemical and hydrogen isotope evidence for in site dehydrogenation of biotite in silicic magma chambers. Geology, 24, 1021–1024.

Foley, S.F. (1989) Experimental constraints on phlogopite chemistry in lamproites: 1. The effect of water activity and oxygen fugacity. European Journal of Mineralogy, 1, 411–426.

Franzini, M., Leoni, L., and Saitta, M. (1975) Revisione di una metodologia analitica per fluorescenza-X, basata sulla correzione completa degli effetti di matrice. Rendiconti della Società Italiana di Mineralogia e Petrografia, 31, 365–379.

Fujinawa, A. and Green, T.H. (1997) Partitioning behaviour of Hf and Zr between anphibole, clinopyroxene, garnet and silicate melts at high pressure. European Journal of Mineralogy, 9, 379–391.

Grunder, A.L. (1987) Low $\delta^{18}O$ silicic volcanic rocks at the Calabozos Caldera Complex, southern Andes—Evidence for upper crustal contamination. Contributions to Mineralogy and Petrology, 95, 71–81.

Guidotti, C.V. (1984) Micas in metamorphic rocks. In P.H. Ribbe, Ed., Micas, 13, p. 357–468. Reviews in Mineralogy, Mineralogical Society of America, Chantilly, Virginia.

Guidotti, C.V. and Sassi, F.P. (2002) Constraints on studies of metamorphic K-Na white micas. In A. Mottana, P.F. Sassi, J.B. Thompson, Jr., and S. Guggenheim,

Eds., Micas: Crystal Chemistry and Metamorphic Petrology, 46, p. 413–448. Reviews in Mineralogy and Geochemistry, Mineralogical Society of America, Chantilly, Virginia.

Harangi, S., Mason, P.R.D., and Lukacs, R. (2005) Correlation and petrogenesis of silicic pyroclastic rocks in the Northern Pannonian Basin, Eastern-Central Europe: In situ trace element data of glass shards and mineral chemical constraints. Journal of Volcanology and Geothermal Research, 143, 237–257.

Hildreth, W., Christiansen, R.L., and O'Neil, J.R. (1984) Catastrophic isotopic modifications of rhyolitic magma at times of caldera subsidence, Yellowstone Plateau volcanic field. Journal of Geophysical Research, 89, B8339–B8369.

Irvine, T.N. and Baragar, W.R.A. (1971) A Guide to the Chemical Classification of the Common Volcanic Rocks. Canadian Journal of Earth Sciences, 8, 523–548.

Jeong, G.Y. and Kim, H.B. (2003) Mineralogy, chemistry, and formation of oxidized biotite in the weathering profile of granitic rocks. American Mineralogist, 88, 352–364.

Jolivet, L., Faccenna, C., Goffé, B., Mattei, M., Rosseti, F., Brunet, C., Storti, F., Funiciello, R., Cadet, J.P., d'Agostino, N., and Parra, T. (1998) Midcrustal shear zones in postorogenic extension: example from the Tyrrhenian Sea. Journal of Geophysical Research, 103, 12123–12160.

King, P.L., Hervig, R.L., Holloway, J.R., Vennemann, T.W., and Righter, K. (1999) Oxy-substitution and dehydrogenation in mantle-derived amphibole megacrysts. Geochimica et Cosmochimica Acta, 63, 3635–3651.

Kleiman, L.E., Saragovi, C., Puglisi, C., and Labenski de Kanter, F. (1992) Biotite oxidation processes in ash-flow tuffs (Mendoza, Argentina): A Mössbauer spectroscopy and chemical study. Chemical Geology, 97, 251–264.

Knight, J.E. (1977) A thermochemical study of alunite, enargite, luzonite, and tennantite deposits. Economic Geology, 72, 1321–1336.

Kogure, T. (2002) Investigation of micas using advanced Transmission Electron Microscopy. In A. Mottana, P.F. Sassi, J.B. Thompson, Jr., and S. Guggenheim, Eds., Micas: Crystal Chemistry and Metamorphic Petrology, 46, p. 281–312. Reviews in Mineralogy and Geochemistry, Mineralogical Society of America, Chantilly, Virginia.

Kogure, T. and Nespolo, M. (2001) Atomic structures of planar defects in oxybiotite. American Mineralogist, 86, 336–340.

Le Bas, M.I., Le Maitre, R.W., and Wolley, A.R. (1992) The construction of the total alkali-silica chemical classification of volcanic rocks. Mineralogy and Petrology, 46, 1–22.

Leoni, L. and Saitta, M. (1976) X-ray fluorescence analysis of 29 trace elements in rock and mineral standards. Rendiconti della Società Italiana di Mineralogia e Petrografia, 32, 497–510.

Mesto, E., Schingaro, E., Scordari, F., and Ottolini, L. (2006) An electron microprobe analysis, secondary ion mass spectrometry, and single-crystal X-ray diffraction study of phlogopites from Mt. Vulture, Potenza, Italy: Consideration of cation partitioning. American Mineralogist, 91, 182–190.

Miyagi, I., Matsubaya, O., and Nakashima, S. (1998) Change in D/H ratio, water content and color during dehydration of hornblende. Geochemical Journal 32, 33–48.

Murphy, S.F., Brantley, S.L., Blum, A.E., White, A.F., and Dong, H. (1998) Chemical weathering in a tropical watershed, Luquillo Mountains, Puerto Rico: II. Rate and mechanism of biotite weathering. Geochimica et Cosmochimica Acta, 62, 227–243.

Negretti, G.C., Lombardi, G., and Morbidelli, L. (1966) Studio geo-petrografico del settore vulcanico Tolfetano–Cerite (Lazio—IV. Le manifestazioni vulcaniche acide del settore Civitavecchiese–Tolfetano, 172 p. Istituto di Petrografia Università degli Studi di Roma, Italy.

Oba, T., Yagi, K., and Hariya, Y. (1986) Stability relation of kaersutite, reinvestigated on natural and synthetic samples. In Morphology and Phase Equilibria of Minerals, Proceedings of the 13th General Meeting IMA, Varna, September 19th–25th, 1982. Bulgarian Academy of Sciences, Sofia, Bulgaria, 353–363.

Ohta, T., Takeda, H., and Takeuchi, Y. (1982) Mica polytypism: similarities in the crystal structures of coexisting 1*M* and $2M_1$ oxybiotite. American Mineralogist, 67, 298–310.

Pallister, J.S., Hoblitt, R.P., and Reyes, A.G. (1992) A basalt trigger for the 1991 eruptions of Pinatubo volcano? Nature, 356, 426–428.

Pinarelli, L. (1991) Geochemical and isotopic (strontium, lead) evidence of crust-mantle interaction in acidic melts. The Tolfa-Cerveteri-Manziana volcanic complex (central Italy): a case history. Chemical Geology, 92, 177–195.

Rancourt, D.G., Mercier, P.H.J., Cherniak, D.J., Desgreniers, S., Kodama, H., Robert, J-L., and Murad, E. (2001) Mechanisms and crystal chemistry of oxidation in annite: resolving the hydrogen-loss and vacancy reactions. Clays and Clay Minerals, 49, 455–491.

Rebertus, R.A., Weed, S.B., and Buol, S.W. (1986) Transformation of biotite to kaolinite during saprolite-soil weathering. Soil Science Society of America Journal, 50, 810–819.

Redhammer, G.J., Dachs, E., and Amthauer, G. (1995) Mössbauer spectroscopic and X-ray powder diffraction studies of synthetic micas on the join Annite $KFe_3AlSi_3O_{10}(OH)_2$–phlogopite $KMg_3AlSi_3O_{10}(OH)_2$. Physics and Chemistry of Minerals, 22, 282–294.

Redhammer, G.J., Beran, A., Schneider, J., Amthauer, G., and Lottermoser, W. (2000) Spectroscopic and structural properties of synthetic micas on the annite–siderophyllite binary: Synthesis, crystal structure refinement, Mössbauer and infrared spectroscopy. American Mineralogist, 85, 449–465.

Redhammer, G.J., Amthauer, G., Lottermoser, W, Bernroider, M., Tippelt, G., and Roth, G. (2005) X-ray powder diffraction and ^{57}Fe–Mössbauer spectroscopy of synthetic trioctahedral micas $\{K\}[Me_3]\langle TSi_3\rangle O_{10}(OH)_2$, Me = Ni^{2+}, Mg^{2+}, Co^{2+}, Fe^{2+}; T = Al^{3+}; Fe^{3+}. Mineralogy and Petrology, 85, 89–115.

Rowins, S.M., Lalonde, A.E., and Cameron, E.M. (1991) Magmatic oxidation in the syenitic Murdock Creek Intrusion, Kirkland Lake, Ontario: evidence from the ferromagnesian silicates. Journal of Geology, 99, 395–414.

Sato, M. and Wright, T.C. (1966) Oxygen fugacities directly measured in magmatic gases. Science, 153, 1103–1105.

Schingaro, E., Scordari, F., and Ventruti, G. (2001) Trioctahedral micas-1*M* from Mt. Vulture (Italy): structural disorder and crystal chemistry. European Journal of Mineralogy, 13, 1057–1069.

Shane, P., Smith, V., and Nairn, I. (2003) Biotite composition as a tool for the identification of Quaternary tephra beds. Quaternary Research, 59, 262–270.

Sheldrick, G.M. (1997) SHELX-97, program for crystal structure determination. University of Göttingen, Germany.

Sparks, R.S.J., Sigurdsson, H., and Wilson, L. (1977) Magma mixing: A mechanism for triggering acid explosive eruptions. Nature, 267, 315–318.

Takeda, H. and Ross, M. (1975) Mica polytypism: dissimilarities in the crystal structures of coexisting 1*M* and $2M_1$ biotite. American Mineralogist, 60, 1030–1040.

Virgo, D. and Popp, R.K. (2000) Hydrogen deficiency in mantle-derived phlogopites. American Mineralogist, 85, 753–759.

Wallace, M.E. and Green, D.H. (1991) The effect of bulk rock composition on the stability of amphibole in the Upper Mantle: Implications for solidus positions and mantle metasomatism. Mineralogy and Petrology, 44, 1–19.

Wones, D.R. and Eugster, H.P. (1965) Stability of biotite: Experiment, theory and application. American Mineralogist, 50, 1228–1272.

Manuscript received June 6, 2006
Manuscript accepted November 16, 2006
Manuscript handled by G. Diego Gatta